Research Article Vol. 1, No. 8 / 15 Aug 2022 / Optics Continuum 1668
OPTICS CONTINUUM

Integrated photonics approach to radio-frequency self-interference cancellation

AWANISH PANDEY,* KASPER VAN GASSE, AND DRIES VAN THOURHOUT

Ghent University-imec, Department of Information Technology, Technologiepark-Zwijnaarde 15, 9052 Gent, Belgium
*awanish.pandey@ugent.be

Abstract: An integrated photonics based scheme for radio-frequency self-interference cancellation is proposed and demonstrated. It is achieved using a dual-parallel Mach-Zehnder modulator that eliminates the interference signal in the optical domain. The output of the modulator is a carrier suppressed double-sideband waveform that contains only the signal of interest. Finally, the signal of interest is recovered by combining the modulator output with a local optical carrier and detecting it at a high-speed photodetector. We present a detailed theoretical analysis and derive the optimal condition for self-interference cancellation for small modulation indices. The modulators were designed and fabricated on IMEC's Silicon-on-Insulator iSiPP50G platform. Using this technique, we experimentally obtain a cancellation depth of 30 dB and a signal to interference ratio of 25 dB for frequencies up to 20 GHz, limited only by the equipment used. This is the first demonstration of self-interference cancellation on a silicon photonics platform and a further expansion of the functionalities offered by integrated microwave photonics.

1. Introduction

Radio-over-fiber (RoF) technology has attracted considerable interest in the past few years as it promises to facilitate high bandwidth, low latency, electromagnetic interference immune, and sustainable connectivity between devices operating at radio frequencies (RF) [1]. In this technology, the radio signal is modulated over an optical carrier, the required signal processing is carried out in the optical domain and the signal is then transported to the remote radio heads. Finally, the signal is demodulated to recover the microwave signal, is amplified to the desired signal strength, and is passed on to an antenna for the last mile connection. Traditionally, the uplink (transmitted by the user) and downlink (received) microwave frequencies from the base station (BS) are different to avoid any self-interference [2–4]. Self-interference arises due to the direct reception of the downlink signal by the uplink receiver as shown in Fig. 1. Since the uplink signal is subsequently transmitted to the central office (CO), self-interference degrades the quality of the signal received at the CO. Though different frequency operation alleviates self-interference, the spectrum efficiency can be doubled if the uplink and downlink frequencies are kept identical (in-band). Given the ever-increasing demand for higher data rates, in-band radio communication channels are being explored with an emphasis on self-interference cancellation (SIC) at the BS [5].

Microwave photonics based implementations of SIC have garnered considerable interest owing to their large bandwidth of operation, low-loss, and cost-effectiveness. For example, in [6–13] SIC was achieved for single frequency and wideband signals using a dual-parallel Mach-Zehnder modulator (DPMZM) as well as series of MZMs by driving the modulators with the interference signal and adjusting the bias of each modulator to reduce the output power of the interference signal. In [14], SIC was achieved by creating a matched copy of the interference signal using optical attenuators and tunable optical delay units and later subtracting it from the received signal. Other methods include using electro-absorption modulators and a balanced photodetector [15],

#461004 https://doi.org/10.1364/OPTCON.461004
Journal © 2022 Received 11 Apr 2022; revised 10 Jul 2022; accepted 11 Jul 2022; published 25 Jul 2022

OPTICS CONTINUUM

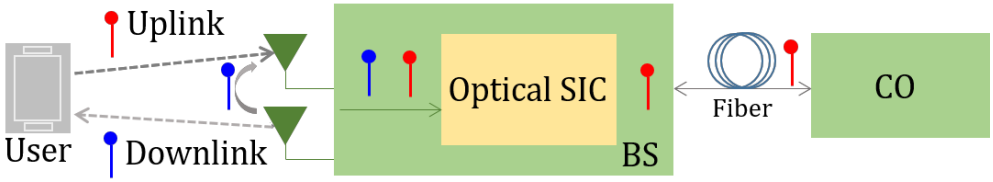

Fig. 1. Optical domain SIC concept. The BS receives both interference and the signal of interest. The interference signal is removed in the optical domain and the signal of interest is further transmitted to CO. BS: base station, CO: central office.

and parallel polarization modulators [16]. DPMZMs have also been explored for adaptive control and cancellation by including an amplifier in one of the Mach-Zehnder arms and using the RF output as a feedback to control the amplification with the help of complex algorithms [17]. In the aforementioned solutions, the self-interference is mitigated in the optical domain and the recovered microwave signal is free from any interference signal. However, such SIC units have been built using discrete fiber-optic components that have high cost, occupy large space, and are not easily portable.

These challenges can be overcome by exploring integrated photonics based SIC solutions as they have a smaller footprint, consume less power, and as they rely on mature fabrication processes from the CMOS industry, can be mass manufactured cost-effectively. Chip scale photonics is already a well-established field that has found its applications in a variety of fields [18]. However, there has been only one integrated photonics based demonstration for microwave SIC [19,20]. It was realized on an InP material platform and entails two lasers, a balanced photodetector, and three amplifiers and offers SIC over a frequency range of 6 GHz. Given the unique advantages offered by silicon platforms, such as low-loss transmission at telecommunication wavelengths, it would be highly advantageous to explore SIC also on this platform [21].

In this letter, for the first time, we demonstrate narrowband RF SIC on a silicon-on-insulator platform, using a DPMZM. Although the design could in principle also be used for wideband RF cancellation, we restrict the discussion to narrowband RF in this work owing to the limited availability of RF components in the lab. The schematic of the DPMZM is shown in Fig. 2(a). It consists of two child MZMs placed in each arm of a parent MZI. The design of the child MZMs is based on the single drive series push-pull traveling wave MZM described in [22]. The modulators are realized with lateral pn-junction phase shifters using the iSiPP50G silicon photonics platform of IMEC [23]. The pn-doped waveguides of the child MZMs are closely placed together and are driven using a single traveling wave electrode. The push-pull configuration is achieved by connecting the pn-junctions of each arm of the child MZIs in series with opposite polarity. The electrodes are terminated with a 50 Ohm resistor to avoid any unwanted microwave signal reflections. The bias for the child MZMs is provided by a separate biasing contact using a long metal trace (B1, B2 in Fig. 2(a)). Thermo-optic phase shifters, with a common ground, are placed on each arm of the child and parent interferometers. Static bias to the child MZMs and parent MZI is provided using these phase shifters. The dc pads are grouped on one side of the device and are wire-bonded to a carrier substrate for easier control. The RF signal is provided to the child MZMs using a high-speed GSSG probe. The DPMZM is realized using 450 nm × 220 nm single-mode silicon waveguides, and six multi-mode interferometers acting as power splitter/combiners. Light is coupled in and out of the device using fiber-to-chip grating couplers with 6dB/coupler loss. A microscope image of the wire-bonded chip along with the high-speed probe and the optical fibers used for coupling light in and out of the chip is shown in Fig. 2(b). A microscope image of the fabricated device is shown in Fig. 2(d) and the passive transmission is shown in Fig. 2(c). The insertion loss of the pn-doped waveguide is 3 dB/cm. We measured the

OPTICS CONTINUUM

half wave voltage V_π of the child MZMs to be 15 V. Taking into account the geometrical length of the doped region in the child MZMs, 1.6 mm, this is equivalent with a $V_\pi L$ of 2.4 V cm.

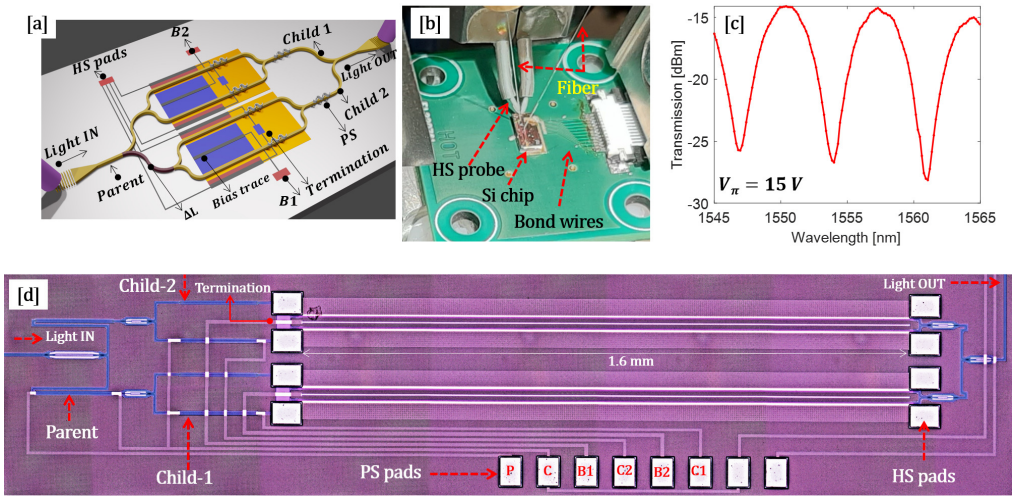

Fig. 2. Design and response of DPMZM, (a) schematic of DPMZM, (b) measurement setup with electrical connections and optical fibers, (c) passive transmission, and (d) microscope image of DPMZM. P: thermo-optic phase tuner pad for the parent MZI, C: common ground pad for child and parent MZI, B1, B2: bias pads for child-2 and child-1 respectively, C1 and C2: pads for thermo-optic tuners for the child MZMs.

We first explain the working principle and derive the necessary conditions for the DPMZM to achieve SIC. The uplink signal, which is the signal-of-interest (SOI), is denoted as $V_{SOI}(t)$ while the interference signal (downlink signal) is denoted as $V_I(t)$. Child-1 MZM is driven by the corrupted signal $(V_{SOI}(t) + V_I(t))$ and Child-2 MZM is driven by an attenuated version of the interference signal, which we refer to as the reference signal, $V_R(t)$. The SOI, interference, and reference signals can be expressed as:

$$V_{SOI}(t) = A_1 \cos(\Omega t + \phi_1 t) \tag{1}$$

$$V_I(t) = A_2 \cos(\Omega t + \phi_2 t) \tag{2}$$

$$V_R(t) = A_3 \cos(\Omega t + \phi_3 t) \tag{3}$$

The interference and reference signals will have different amplitudes and phase. However, their phase can be made identical by introducing an RF time delay to make $\phi_2 = \phi_3$. The output from the DP-MZM for an input optical carrier $S_{in} = Ae^{\iota\omega_l t}$ is then given by:

$$\begin{aligned}\frac{E_{out}(t)}{A} = \frac{1}{\sqrt{2}} \cos(\alpha_1 + \beta_1 \cos(\Omega t + \phi_1(t)) + \beta_2 \cos(\Omega t + \phi_2(t))) \\ \times e^{j\omega_l t} + \frac{1}{\sqrt{2}} \cos(\alpha_2 + \beta_3 \cos(\Omega t + \phi_2(t))) \times e^{j\theta + j\omega_l t}\end{aligned} \tag{4}$$

where $\alpha_{1,2} = \frac{\pi V_{1,2}}{V_\pi}$ with $V_{1,2}$ the bias applied on the child MZMs, $\beta_{1,2,3} = \frac{\pi A_{1,2,3}}{V_\pi}$ the modulation index with $A_{1,2,3}$ the SOI, interference, and reference RF amplitudes in volts, and $\theta = \frac{2\pi n_{eff}\Delta L}{\lambda} + \frac{\pi V_3}{V_\pi}$. ΔL is the path length difference between the two arms of the parent MZI and V_3 is the voltage applied on the parent MZI thermo-optic phase shifter. Performing Jacobi-Anger expansion of

OPTICS CONTINUUM

Eq. (4) under the approximation that $\beta_{1,2,3}<<1$ and retaining only first order sideband terms leads to the condition for self-interference as:

$$-exp(j\theta)\sin(\alpha_2)J_1(\beta_3) = \sin(\alpha_1)J_0(\beta_1)J_1(\beta_2) \tag{5}$$

Under this condition, the output of the DPMZM will be independent of ϕ_2 and ϕ_3. In the limiting case when $\theta = \pi$, and $\alpha_2 = \alpha_1$, Eq. (5) becomes:

$$J_1(\beta_3) = J_0(\beta_1)J_1(\beta_2) \tag{6}$$

which was also derived in Ref. [6,7]. However, Eq. (5) is general and can be applied for a range of bias points as long as the MZMs are weakly modulated. Under this condition, assuming unit amplitude for the input optical signal at a frequency ω_l, the output of the DPMZM takes the form:

$$E_{out}(t) = \frac{J_0(\beta_2)J_1(\beta_1)}{\sqrt{2}}\cos(\Omega t + \phi_1(t))exp(j\omega_l t) \tag{7}$$

For small arguments, the Bessel functions can be approximated as $J_n(\beta) = \frac{1}{n!}\left(\frac{\beta}{2}\right)^n$, allowing to further simplify Eq. (7) to $E_{out}(t) = \frac{\beta_1}{2\sqrt{2}}\cos(\Omega t + \phi_1(t))exp(j\omega_l t)$. Equation (7) represents a carrier suppressed double sideband signal with the desired uplink signal information in the sidebands. Finally, the carrier suppressed signal is combined with an attenuated optical carrier tapped from the input laser to give a double sideband with carrier signal. The optical output is then written as:

$$E_{final}(t) = \frac{\beta_1}{2\sqrt{2}}\cos(\Omega t + \phi_1(t))exp(j\omega_l t) + Bexp(j\omega_l t) \tag{8}$$

where B is the amplitude of the tapped optical carrier from the input laser which is combined with the carrier suppressed signal from the DPMZM. In this way, the uplink RF signal can be retrieved by applying the DPMZM output, combined with the tapped optical carrier, at the photo-detector. The output optical signal can suffer from a power fading effect from BS to CO due to optical fiber dispersion. This can mitigated by including a polarization controller at the DP-MZM output and providing a static phase shift to the optical carrier [7].

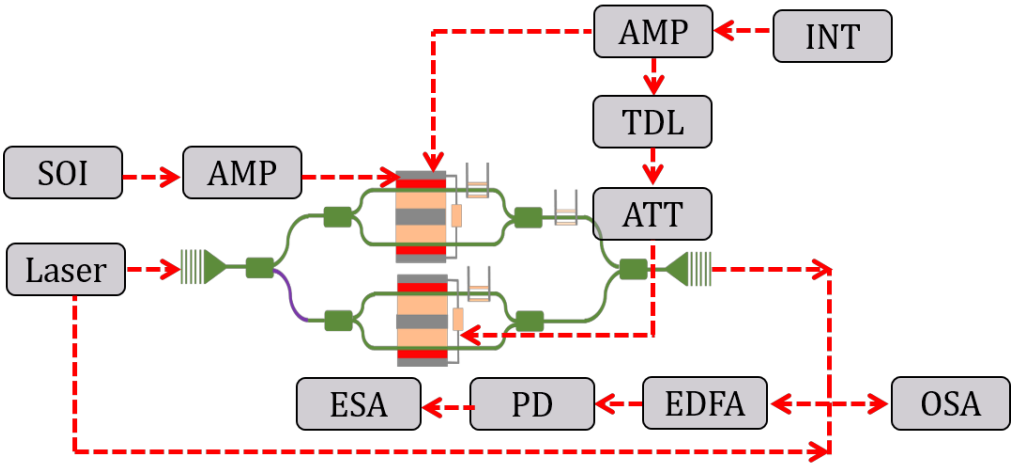

Fig. 3. SIC experimental setup. AMP: RF amplifier, TDL: time delay unit, EDFA: Erbium doped fiber amplifier, ATT: attenuator, PD: photo-detector, and ESA: electrical spectrum analyzer.

OPTICS CONTINUUM

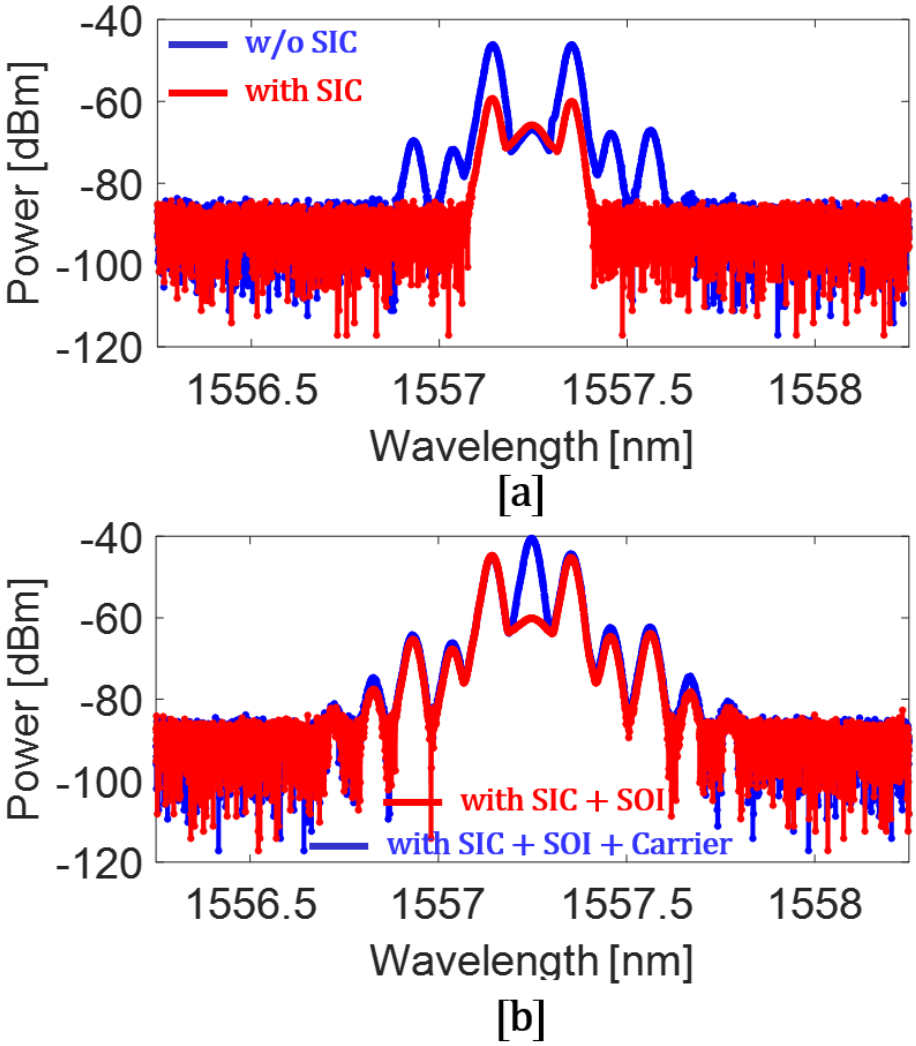

Fig. 4. Optical response of the DPMZM (a) without SIC (only $V_I(t)$ applied on Child 2) and with SIC ($V_I(t)$ applied on Child-2 and $V_R(t)$ on Child 1) (b) SOI with SIC enabled ($V_I(t) + V_R(t) + V_{SOI}(t)$) when the reference laser is ON and OFF.

The experimental setup is shown in Fig. 3. A continuous wave tunable laser (Santec 510) acts as the optical input to the DPMZM. The RF port of the child-1 MZM is driven by the interference signal as well as the SOI ($V_{SOI}(t) + V_I(t)$). The interference signal and SOI are generated from two different RF sources (Rohde & Schwarz SMB 100A and SMR40) and are amplified before being applied to the device. The bandwidth of the amplifiers used for the SOI and interference signal is 15 GHz and 60 GHz respectively. The MZMs are reverse biased at 3 V. The RF port of the child-2 MZM is driven by the interference signal after passing it through a time delay unit (Spectrum C3117) and an RF attenuator. We maintain $\alpha_2 = \alpha_1$ by the 3 V bias of the MZMs leading to Eq. (6) and the time delay unit is used to make the phase of the interference and reference signals equal. The applied RF signals have $\beta_1 = 0.36$, $\beta_2 = 0.33$, and $\beta_3 = 0.32$, which closely satisfies Eq. (6). The carrier-suppressed double sideband output from the DPMZM is

OPTICS CONTINUUM

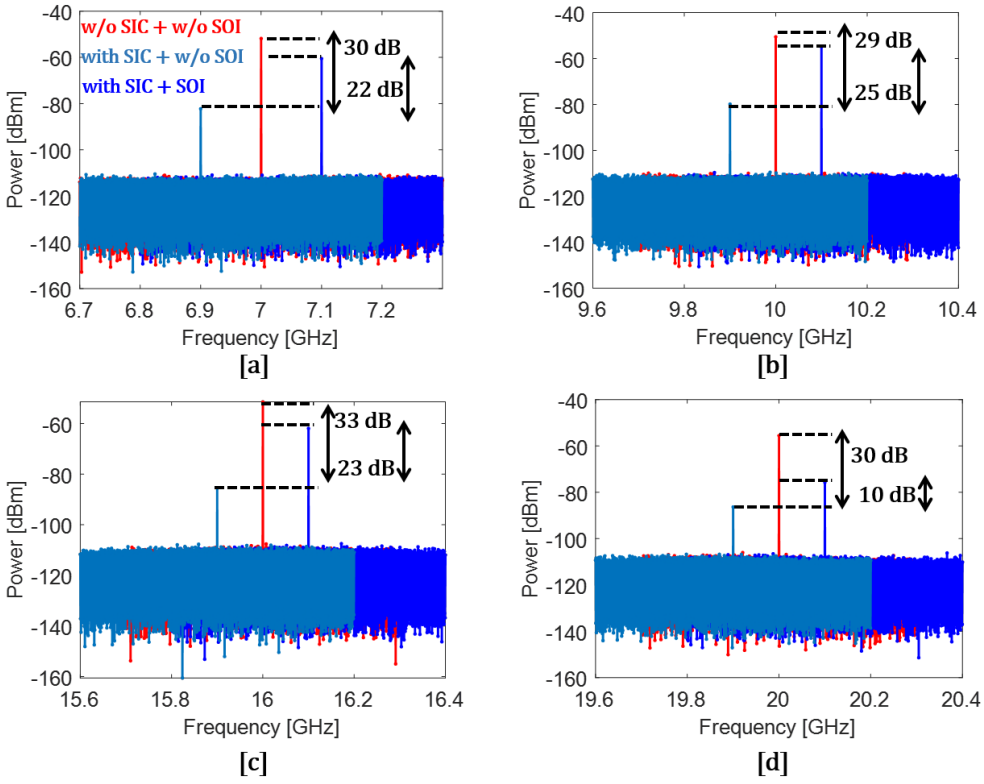

Fig. 5. Electrical spectra of the single frequency signal from the photodetector with and without SIC and SOI when the RF frequency is (a) 7 GHz, (b) 10 GHz, (c) 16 GHz, and (d) 20 GHz. The signals are shifted by 0.1 GHz for better representation

recorded using an OSA. For the RF domain analysis, it is combined with the tapped optical carrier from the input laser, and inspected on an ESA.

The optical spectrum recorded on the OSA (Anritsu MS9740A) is shown in Fig. 4. Figure 4(a) shows the output from the DPMZM when the SIC is disabled (interference signal applied only to child-1 MZM) and when it is enabled (interference signal applied to both child MZMs). With the SIC disabled, the interference signal modulates child-1 MZM resulting in a carrier suppressed double sideband signal. This is also suggested from our theoretical analysis. The carrier is not completely suppressed due to the small extinction ratio of the interference pattern generated by the DPMZM (12 dB). Since the modulation index is small, the second order sideband is 26 dB smaller than the first order. When SIC is enabled, the optical power in the sidebands reduces by 14 dB. This demonstrates the interference signal indeed has been suppressed in the optical domain. Figure 4(b) shows the output when also the SOI, with SIC enabled, is applied to Child-1. Since the interference signal is suppressed, the sidebands contain the SOI information. Before supplying this signal to the PD, the optical carrier, tapped from the input laser, is added to it using an optical coupler. Figure 4(b) also shows the final output, a double sideband signal with optical carrier.

Figure 5 shows the obtained RF signal at the PD for three conditions: only $V_I(t)$ applied on Child-1 MZM (no SOI, no SIC), $V_I(t)$ applied on Child-1 MZM, $V_R(t)$ applied on Child-2 MZM (with SIC and without SOI), and with SIC and with SOI, for different RF frequencies. The signals are separated by 0.1 MHz for clear representation. Two key parameters are labeled in the figure. First, the cancellation depth of the interference signal, which is the measure of the power

OPTICS CONTINUUM

reduction in the interference signal power when SIC is enabled. It remains in the range of 30 dB till 20 GHz. The second parameter is the difference between the power level of the SOI and the remaining interference signal, the signal to interference ratio, with SIC enabled. We obtain this parameter to be in the range of 25 dB till 16 GHz of operation and it falls to 10 dB at 20 GHz. We attribute this reduction to the limited bandwidth of the SOI RF amplifier. At 20 GHz, the output of the SOI RF amplifier is just 10 dBm ($V_{pp} = 2V$).

In summary, a silicon photonics based approach for RF self-interference cancellation was proposed and demonstrated for in-band radio over fiber systems. The cancellation was achieved in the optical domain using a dual-parallel Mach-Zehnder modulator and a cancellation depth of 33 dB is achieved experimentally. The modulator was fabricated in the IMEC CMOS pilot line and offers a path towards mass manufacturing and large-scale system integration. A theoretical model was developed and the necessary conditions for optimal performance were derived. We believe this first silicon photonics based demonstration of interference cancellation will pave the way for future research work in this field.

Funding. H2020 Future and Emerging Technologies (732894).

Disclosures. The authors declare no conflicts of interest.

Data availability. Data for the results presented in this paper can be obtained from the authors upon reasonable request.

References

1. C. Lim, Y. Tian, C. Ranaweera, T. A. Nirmalathas, E. Wong, and K. L. Lee, "Evolution of Radio-Over-Fiber Technology," J. Lightwave Technol. **37**(6), 1647–1656 (2019).
2. K. Kolodziej, B. Perry, and J. Herd, "In-band full-duplex technology: Techniques and systems survey," IEEE Trans. Microw. Theory Tech. **67**(7), 3025–3041 (2019).
3. R. Aksar, J. Chung, Z. Guo, H. Ko, W. Keugsen, and T. Haustein, "Interference handling challenges toward full duplex evolution in 5G and beyond cellular networks," IEEE Wireless Commun. **28**(1), 51–59 (2021).
4. I. P. Roberts, J. G. Andrews, H. B. Jain, and S. Vishwanath, "Millimeter-Wave Full Duplex Radios: New Challenges and Techniques," IEEE Wireless Commun. **28**(1), 36–43 (2021).
5. D. Yang, H. Yuksel, and A Molnar, "A wideband highly integrated and widely tunable transceiver for in-band full-duplex communication," IEEE J. Solid-State Circuits **50**(5), 1189–1202 (2015).
6. Y. Chen and S. Pan, "Simultaneous wideband radio-frequency self-interference cancellation and frequency downconversion for in-band full-duplex radio-over-fiber systems," Opt. Lett. **43**(13), 3124 (2018).
7. Y. Chen, "A photonic-based wideband RF self-interference cancellation approach with fiber dispersion immunity," J. Lightwave Technol. **38**(17), 4618–4624 (2020).
8. Y. Zhang, S. Xiao, H. Feng, L. Zhang, Z. Zhou, and W. Hu, "Self-interference cancellation using dual-drive Mach-Zehnder modulator for in-band full-duplex radio-over-fiber system," Opt. Express **23**(26), 33205 (2015).
9. X. Han, B. Huo, Y. Shao, and M. Zhao, "Optical RF self-interference cancellation by using an integrated dual-parallel MZM," IEEE Photonics J. **9**, 1 (2017).
10. B. Weng, Y. Chen, and Y. Chen, "Photonic-assisted wideband frequency downconverter with self-interference cancellation and image rejection," Appl. Opt. **58**(13), 3539 (2019).
11. J. Wang, Y. Wang, Z. Zhang, Z. Zhao, and J. Liu, "Optical self-interference cancellation with frequency downconversion based on cascade modulator," IEEE Photonics J. **12**(6), 1–12 (2020).
12. Y. Chen and J. Yao, "Photonic-assisted RF self-interference cancellation with improved spectrum efficiency and fiber transmission capability," J. Lightwave Technol. **38**(4), 761–768 (2019).
13. X. Han, B. Huo, Y. Shao, C. Wang, and M. Zhao, "RF self-interference cancellation using phase modulation and optical sideband filtering," IEEE Photonics Technol. Lett. **29**(11), 917–920 (2017).
14. J. J. Sun, M. P. Chang, and P. R. Prucnal, "Demonstration of over-the-air RF self-interference cancellation using an optical system," IEEE Photonics Technol. Lett. **29**(4), 397–400 (2017).
15. M. Change, M. Fok, A. Hofmaier, and P. Prucnal, "Optical analog self-interference cancellation using electro-absorption modulators," IEEE Microw. Wireless Compon. Lett. **23**(2), 99–101 (2013).
16. W. Zhou, P. Xiang, Z. Niu, M. Wang, and S. Pan, "Wideband optical multipath interference cancellation based on a dispersive element," IEEE Photonics Technol. Lett. **28**(8), 849–851 (2016).
17. M. P. Chang, C. L. Lee, W. Wu, and P. R. Prucnal, "Adaptive optical self-interference cancellation using a semiconductor optical amplifier," IEEE Photonics Technol. Lett. **27**(9), 1018–1021 (2015).
18. C. R. Pollock and M. Lipson, *Integrated Photonics* (Kluwer Academic Publishers, 2003).
19. M. P. Chang, E. C. Blow, J. J. Sun, M. Z. Lu, and P. R. Prucnal, "Integrated microwave photonic circuit for self-interference cancellation," IEEE Transactions on Microw. Theory Tech. **65**(11), 4493–4501 (2017).

OPTICS CONTINUUM

20. M. P. Chang, E. C. Blow, M. Z. Lu, J. J. Sun, and P. R. Prucnal, "RF characterization of an integrated microwave photonic circuit for self-interference cancellation," IEEE Transactions on Microw. Theory Tech. **66**(1), 596–605 (2017).
21. D. Thomson, A. Zilkie, J. E. Bowers, T. Komljenovic, G. T. Reed, L. Vivien, D. Marris-Morini, E. Cassan, L. Virot, J. M. Fedeli, and J. M. Hartman, "Roadmap on silicon photonics," J. Opt. **18**(7), 073003 (2016).
22. A. Samani, M. Chagnon, D. Patel, V. Veerasubramanian, S. Ghosh, M. Osman, Q. Zhong, and D. Plant, "A low-voltage 35-GHz silicon photonic modulator-enabled 112-Gb/s transmission system," IEEE Photonics J. **7**(3), 1–13 (2015).
23. M. Pantouvaki, S. A. Srinivasan, Y. Ban, P. De Heyn, P. Verheyen, G. Lepage, H. Chen, J. De Coster, N. Golshani, S. Balakrishnan, P. Absil, and J. Van Campenhout, "Active Components for 50 Gb/s NRZ-OOK Optical Interconnects in a Silicon Photonics Platform," J. Lightwave Technol. **35**(4), 631–638 (2017).